EFFECTS OF LATTICE MISMATCH STRAIN ON Fe8N-Fe16N2 PHASE TRANSFORMATION AND AGING PROCESS

A THESIS
SUBMITTED TO THE FACULTY OF THE GRADUATE SCHOOL
OF THE UNIVERSITY OF MINNESOTA
BY

YIMING WU

IN PARTIAL FULFILLMENT OF THE REQUIREMENTS
FOR THE DEGREE OF
MASTER OF ELECTRICAL ENGINEERING

JIAN-PING WANG

DECEMBER 2010

Acknowledgements

First of all, I want to express my appreciation to my advisor, Professor Jian-Ping Wang, who provides me a good opportunity and strong support to make this MSEE thesis work possible. I am so happy that I can be part of this exciting research in his group.

I also would like to thank Professor Anand Gopinath, Professor Steven J. Koester and Professor Rusen Yang as my MSEE thesis examination committee members. I thank Mr. Dave Hultman and staff at ECE machine shop for their great work for the success of my experimental setup.

I want to thank my families and friends for their consistent supports and encouragement during all my high education years. Their love and support keep me moving forward. I also want to thank graduate students, Nian Ji, Haibao Zhao, Hao Wang, Xuan Li, Yisong Zhang, Shihai He, and faculty and staff of the Department of Electrical and Computer Engineering, for all their help.

For my parents and my lover Shuang.

Abstract

It has been debated for decades whether α”-$Fe_{16}N_2$ has a giant saturation magnetization, which couldn’t be predicted by the traditional band magnetic theory. Because of a lot of previous inconsistent research results in the past 40 years, α”-$Fe_{16}N_2$ has been regarded as a debatable mystery material in magnetic research community.

Recently, Wang’s group has successfully rationalized a partially localized 3d electron model based on the first principles calculation and predicted the existence of the giant saturation magnetization in α”-$Fe_{16}N_2$. Furthermore, we have synthesized FeN thin films with partially ordered α”-$Fe_{16}N_2$ phase on GaAs substrate with Fe as the underlayer. Our repeatable experimental results proved the existence of giant saturation magnetization of partially ordered α”-$Fe_{16}N_2$ phase. However, there has been a critical question on this topic for any experimentalist to answer, which has actually bothered magnetic researchers for almost four decades. Why did most experimental research groups not succeed to report the giant saturation magnetization value even with their fabricated FeN films with observed α”-$Fe_{16}N_2$ phase?

This critical question has been answered in this MS thesis work. The effect of the initial strain on the phase transformation between Fe_8N and $Fe_{16}N_2$, which is caused by the lattice mismatch between the FeN layer and its growth template, was investigated. A model was proposed, based on the Johnson-Mehl-Avrami equation, to describe the phase

transformation process between Fe_8N and $Fe_{16}N_2$ phases. Aging effect of the partially ordered $Fe_{16}N_2$ phase, e.g. degradation of giant magnetization behavior vs. time, was analyzed semi-quantitatively. Based on this proposed model, we have successfully rationalized the inconsistency of the fabricated α"-$Fe_{16}N_2$ films by different research groups using different growth technologies.

An integrated facing-target sputtering system has been set up during my MSEE thesis work, which has three pairs of facing targets and ultra high vacuum capability.

Contents

List of Tables

List of Figures

Chapter 1

Introduction

In modern magnetic recording industry, the materials with high saturation magnetization are demanded and playing more and more important roles. By now, several kinds of high saturation magnetization materials, such as Permendurs (FeCo alloys), Hiperco-50 (2% V-FeCo, ordered) and amorphous FeCoB, have been made with saturation magnetizations (Ms) ~ 2 T [1]. Among them, the well known highest saturation material $Fe_{65}Co_{35}$ alloy can reach the highest Ms as 2.45 T. It is also well known that several iron nitrides are magnetic phases, such as α-FeN, ε-$Fe_{2-3}N$ (hcp), γ′-Fe_4N (fcc) [2, 3, 4]. α”-$Fe_{16}N_2$ was reported to possess a giant saturation magnetization value that is much greater than that of Permendurs but most of magnetic research group couldn’t repeat this result and traditional magnetism theory didn’t support this claim too [5].

Jack first found the existence of α”-$Fe_{16}N_2$ phase in the 1951. He reported this iron nitride phase as a metastable phase that was formed from a rapid quenching process from γ′-Fe-N austenite [6]. And in the work of Usikov and Khachaturyan [7], the α”-$Fe_{16}N_2$ phase was reported as an intermediate phase and could not exist stably for a long time. Kim and Takahashi reported to observe a giant saturation magnetization as high as 2.58 T on thin film α”-$Fe_{16}N_2$ phase material that was deposited on glass substrate through a thermal evaporation synthetic process in 1972 [8]. Nakajima et. al. and Russak et. al. both

reported a series of research results on this material [9, 10, 11], especially Sugita et. al., in the 1990s, reported that the single crystal α"-$Fe_{16}N_2$ samples grown epitaxially on GaAs or In doped GaAs substrates by molecule beam evaporation (MBE) could achieve as high as 3.23 T saturation magnetization [12, 13, 14, 15, 16, 17]. Because of its giant saturation magnetization value, this iron nitride phase immediately has attracted a great deal of attentions in the world.

However, many follow-up investigation from independent research groups couldn't achieve the same giant saturation magnetization value as reported by Sugita et. al., based on either powder, bulk or thin film material that contains partially ordered α"-$Fe_{16}N_2$ phase. Only saturation magnetizations less than 2.0 T or about 2.0 T were obtained [18, 19, 20, 21, 22], some others obtained greater saturation magnetization on thin film materials through specially designed thin film deposition processes [23, 24, 25, 26, 27, 28, 29], but still far from the result reported by Sugita et al. Even worse, most of these results seem inconsistent. Since then, α"-$Fe_{16}N_2$ has been regarded as a mystery material in magnetic research community [30]. At the annual conference on Magnetism and Magnetic Materials in 1996, a special symposium was held on the topic $Fe_{16}N_2$, on which both theoreticians and experimentalists presented their work. The papers were published in *J. Appl. Phys.* 79 (1996). No decisive conclusion was drawn on whether it has giant saturation magnetization. Especially, there is no existing theory to rationalize the existence of the giant saturation magnetization. Since then, this research topic has been dropped by most of magnetic researchers.

Recently, Wang's group at the University of Minnesota successfully synthesized α"-$Fe_{16}N_2$ thin film material on GaAs substrate by post-annealing Fe_8N phase that was deposited by a magnetron DC facing-target sputtering technology [31, 32]. Our material growth processes are highly reproducible, and also the thin film component is verified to be consistent through different material characterization technologies. Furthermore, Wang's group has successfully rationalized a partially localized 3d electron model based on the first principles calculation and predicted the existence of the giant saturation magnetization in α"-$Fe_{16}N_2$.

However, there has been a critical question on this topic for any experimentalist to answer, which has actually bothered magnetic researchers for almost four decades. Why did most experimental research groups not succeed to report the giant saturation magnetization value even with their fabrication FeN films with observed α"-$Fe_{16}N_2$ phase?

This critical question has been answered in this MS thesis work. The effect of the initial strain on the phase transformation between Fe_8N and $Fe_{16}N_2$, which is caused by the lattice mismatch between the FeN layer and its growth template, was investigated. A model was proposed, based on the Johnson-Mehl-Avrami equation, to describe the phase transformation process between Fe_8N to $Fe_{16}N_2$ phases. Aging effect of the partially ordered $Fe_{16}N_2$ phase, e.g. degradation of giant magnetization behavior vs. time, was

analyzed semi-quantitatively. Based on this proposed model, we have successfully rationalized the inconsistency of the fabricated α”-$Fe_{16}N_2$ films by different research groups using different growth technologies.

In this thesis, the details of crystalline structure of α”-$Fe_{16}N_2$ is described in Chapter 2, and the Johnson-Mehl-Avrami equation, which is used to quantify ordering-disordering phase transformation behavior is also introduced in the same chapter. Chapter 3 introduces the magnetron DC facing-target sputtering systems (FTS) that include an existing single-pair facing-targets and a three-pair facing-target system (set up through my thesis work) in our lab, which are used to prepare thin film Fe-N samples. The deposition and characterization of Fe-N samples with partially ordered α”-$Fe_{16}N_2$ phase is introduced in Chapter 4. A model is proposed to address the inconsistency of the fabricated α”-$Fe_{16}N_2$ films by different research groups using different growth technologies. In the last chapter, some conclusions based on our results are made and some future research directions are suggested.

Chapter 2

Background

2.1 Crystalline Structure of α'-Fe_8N and α"-$Fe_{16}N_2$ Phases

Figure 2.1 shows the Fe-N phase diagram from ASM handbook [33]. In the phase diagram, the existence of α"-$Fe_{16}N_2$ phase is circled out through the material growth method of Jack [6].

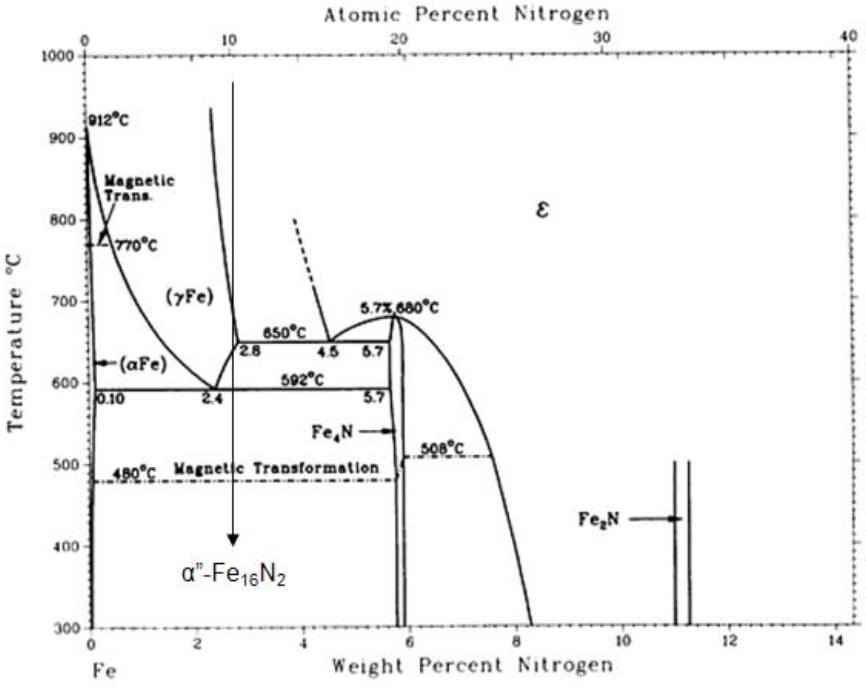

Figure 2.1. The metastable α"-$Fe_{16}N_2$ phase is circled out in the Fe-N phase diagram.

From the previous reports, as shown in Figure 2.2, both α'-Fe_8N and α"-$Fe_{16}N_2$ have body-centered-tetragonal (bct) structures. The difference is that α'-Fe_8N is a chemically disordered phase with randomly located nitrogen atoms, but α"-$Fe_{16}N_2$ phase is an

ordered one, in which nitrogen atoms are located in the a regular position. The lattice parameters for α"-$Fe_{16}N_2$ phase are a = 5.72 Å and c = 6.29 Å, respectively, from Jack's measurement, where a is almost twice the lattice parameter of iron (2.87 Å). These values are slightly variable depending on different Fe-N material growth conditions and also the Fe-N thin film thickness. For the sample by Tanaka et. al., these values were reported as a = 5.72 Å and c = 6.31 Å [34], and Okamoto et. al reported that a varied between 5.70 and 5.71 Å, and c varied between 6.30 and 6.31 Å. These parameters have larger variants for α'-Fe_8N phase. In the same report of Okamoto et. al., a was found to vary from 5.66 Å to 5.70 Å and c from 5.97 Å to 6.28 Å with different nitrogen concentration during Fe-N thin film growth.

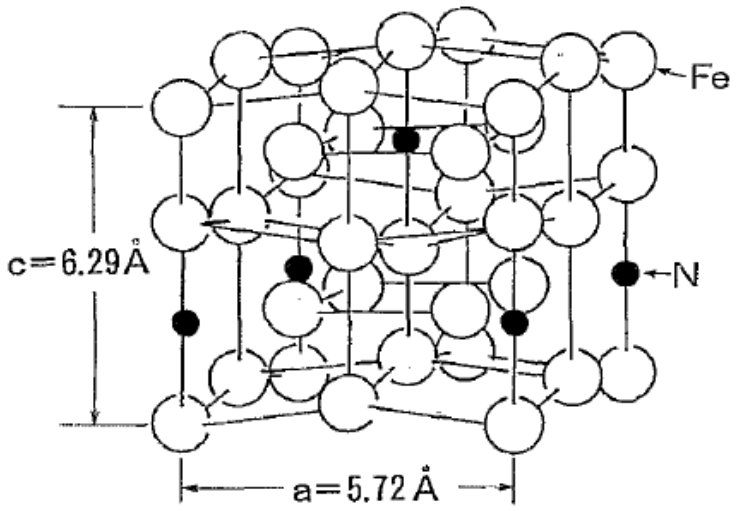

Figure 2.2. The single crystal structure of α"-$Fe_{16}N_2$ is the body-centered-tetragonal, with lattice parameters a = 5.72 Å and c = 6.29 Å [6].

Considering about the ordered α”-$Fe_{16}N_2$ phase, at each nitrogen atom position, the atoms of Fe around the N form an octahedral cluster, which is shown in Figure 2.3. There are three iron sites. Fe8h atoms and Fe4e atoms are inside the octahedral cluster and Fe4d ones are outside the cluster.

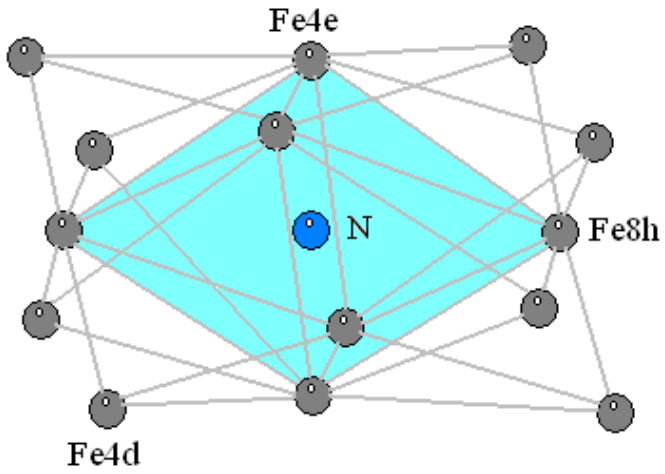

Figure 2.3. In each octahedral cluster that constructed by the atoms of Fe around the N, Fe8h and Fe4e atoms are inside the octahedral cluster and Fe4d ones are outside the cluster.

Typically the prepared FeN samples with α”-$Fe_{16}N_2$ phase have other iron nitrides coexisting. In order to distinguish α”-$Fe_{16}N_2$ phase from other iron nitride, different material characterization techniques could be applied. X-ray diffraction (XRD) is the most common technique to characterize the existence of α”-$Fe_{16}N_2$ phase in the iron nitrides. For the XRD patterns of Fe-N thin film as shown in Figure 2.4 [17], the (002) peaks is a fingerprint peak for α”-$Fe_{16}N_2$ phase. And the integration ratio of X-ray diffraction intensity peaks can be also used to calculate the ordering parameter of nitride

atoms as below [35]:

$$O.P. = I_{\alpha''(002)} / I_{[\alpha''(004)+\alpha'(002)]}. \quad (1)$$

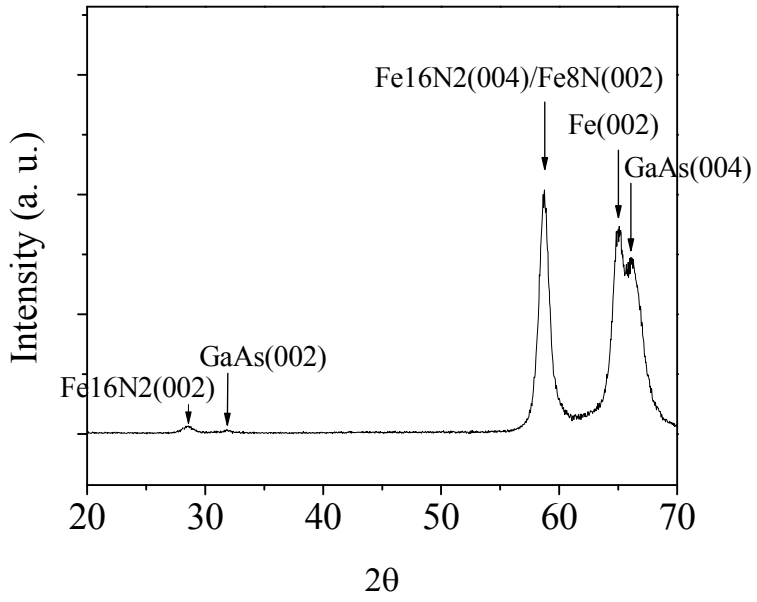

Figure 2.4. The (002) group of intensity peaks are unique for α"-$Fe_{16}N_2$ phase that indicate the existence of this phase and the integration ratio of intensity peaks can be also used to calculate the ordering parameter of nitride atoms.

X-ray Photoelectron Spectroscopy (XPS) is usually used to measure the Fe and N component percentages in the iron nitrides and therefore verify the Fe-N thin film thickness, which includes α'-Fe_8N and α"-$Fe_{16}N_2$ phase [27]. But XPS has difficulty in distinguishing α′-Fe_8N and α"-$Fe_{16}N_2$ phase, because they have the same Fe/N ratio.

2.2 Magnetic Properties of α"-$Fe_{16}N_2$ Phase

Sugita et. al. reported the saturation magnetization values of FeN thin film samples with pure α'-Fe_8N phase, pure α"-$Fe_{16}N_2$ phase and α'-Fe_8N with partial α"-$Fe_{16}N_2$ phase by Vibrating Sample Magnetometer (VSM) [15]. It was found that the saturation magnetization for α'-Fe_8N martensite film is 2.4 T, and for pure α"-$Fe_{16}N_2$ phase sample, that increases obviously to 2.9 T. This value is much larger than that of Permendurs, which is 2.45 T. Even for the sample with partial α"-$Fe_{16}N_2$ phase, which was characterized by XRD, the saturation magnetization value can reach 2.7 T, which is still larger than the value of Permendurs. In the other reported work, the saturation magnetization value of α"-$Fe_{16}N_2$ phase sample reached as high as 3.23 T [16].

Mössbauer spectra is another useful technology to characterize magnetic materials. But it needs to notice that there are different conclusions of using Mössbauer spectra to characterize α"-$Fe_{16}N_2$ phase. Sugita et. al. showed that the Mössbauer spectra of $Fe_{16}N_2$ phase were very similar to that of pure Fe, which seemed contradictory because the magnetic moment of $Fe_{16}N_2$ phase should be much different with that of pure Fe [15], while Borsa and Boerma's research showed the pattern of $Fe_{16}N_2$ phase and pure Fe were different and distinguishable [36]. Also, Borsa and Boerma claimed that the Mössbauer spectra couldn't be used to distinguish the α"-$Fe_{16}N_2$ phase and α′-Fe_8N phase, but Brewer et. al. showed the Mössbauer spectra pattern of pure Fe_8N phase was different from with the combination of $Fe_{16}N_2$ and Fe_8N phase [37]. So far, whether Mössbauer spectra can be used to verify the existence of α"-$Fe_{16}N_2$ phase is still doubtful.

2.3 Thermal Stability of α”-$Fe_{16}N_2$ Phase

The thermal stability of α”-$Fe_{16}N_2$ is very important for practical applications. Sugita et. al. reported that this phase is thermally stable with temperature lower than 300 ˚C [13]. But Jiang et. al. believed that at 200 ˚C, the α”-$Fe_{16}N_2$ phase began to decompose to α-Fe and γ′-Fe_4N phases, until 300 ˚C, the decomposing process was completed [38]. The change of the saturation magnetization with temperature is another method to estimate the thermal stability of α”-$Fe_{16}N_2$ material. Takahashi and Shoji compared the saturation magnetization change with temperature reported by Kim and Takahashi [8], Sugita et al [13] to their own [30]. From the comparison, it was found that the thin film samples with partial α”-$Fe_{16}N_2$ phase that were prepared by Kim and Takahashi was decomposed at 300 ˚C, and the decomposing process finished at 400 ˚C. When the sample was cooled back, α”-$Fe_{16}N_2$ phase started to reform at 250 ˚C, until 150 ˚C, the reformation process finished. The α”-$Fe_{16}N_2$ phase was only reformed partially. For the result of Takahashi and Shoji, it can be seen that the α”-$Fe_{16}N_2$ phase in their samples was decomposed at about 200 ˚C, which agrees with the result of Jiang et. al. And it was transformed to the other phase above 250 ˚C. After the cooling process, the α”-$Fe_{16}N_2$ phase decomposition is irreversible, which is totally different from the result of Kim and Takahashi. For the result of Sugita et. al., the α”-$Fe_{16}N_2$ phase was thermally stable up to 400 ˚C. This result is different from all other reports. Differential scanning calorimetry (DSC) is commonly used to analysis the thermal stability. Tanaka et. al. used DSC to analyze the thermal stability of the α”-$Fe_{16}N_2$ phase [34]. It was found that there was a stage at about 150 ˚C in the DSC pattern of a 0.1 mm thick as-quenched iron plate containing 1.5 mass% N,

which indicated the α”-$Fe_{16}N_2$ phase was precipitated from the decomposition of martensite α′ phase iron nitride. But by now, there is no research of DSC measurement on single phase α”-$Fe_{16}N_2$ samples because DSC measurement usually needs much thicker sample than 1000 $\mathring{A}$, which can’t be achieved by current research works.

The α”-$Fe_{16}N_2$ phase spontaneously aging process under different temperature conditions also belongs to phase thermal stability topic. And it is very important for material industrial application because it is related with material long-term reliability. Because the α’-Fe_8N to α”-$Fe_{16}N_2$ phase transformation is a reversible transformation, after the partially $Fe_{16}N_2$ phase in Fe_8N is formed by annealing, a part of it will transform back to Fe_8N phase spontaneously. The aging process will depend not only on the ordering parameter of the α’-Fe_8N+α”-$Fe_{16}N_2$ sample, but also on the environment temperature and other issues. In order to satisfy the industrial application requirement, α”-$Fe_{16}N_2$ phase has to be relatively stable under different working temperatures for a long time, which means the α”-$Fe_{16}N_2$ phase spontaneously aging process needs to be controlled. By now, there is no reported work in this topic, and in this MS thesis, it will be discussed first time.

2.4 Review of High Magnetic Moment α”-$Fe_{16}N_2$ - Theoretical Research

For the theoretical analysis and simulation on magnetic moment of α”-$Fe_{16}N_2$ phase,

similar to most iron nitrides phases, the magnetism in iron nitrides is generally considered to be based on itinerant ferromagnetism. When the N atom is located in the voids of the iron octahedral clusters as shown in Figure 2.3, to form interstitial compounds, the Fe3d down spin electrons redistribute themselves on different Fe sites because of p-d hybridization between N and its nearest 6 Fe neighbors [39]. But this will fail to predict magnetic moment as high as the reported experimental results [40, 41]. In order to explain the giant magnetic moment mechanism, more models are proposed.

Lai et. al. assumed that there existed a strong correlation effect on all Fe sites in α"-$Fe_{16}N_2$ system and obtained the magnetic moment much closer to the high moment experimental data [42]. However, other researchers couldn't commonly agree that the material system can maintain the properties that gave the high on-site Coulomb U values, so it is hard to guide the future experimental research. Also, Sakuma proposed a high moment charge transfer model [43], which inferred the existence of empty N orbitals near the Fermi level that served as charge hopping sites. This new model can predict a high spin configuration of Fe and also explain the long-range ferromagnetic order through an effective "double exchange" process in the context of highly localized spin interacting configuration. But from the experimental research results, there is no obvious evidence showing that there is much more negatively charged, relative to other iron nitrides. So, there is still some doubting on this model. Recently, Wang's group discovered the localized 3d electron states by X-ray magnetic circular dichroism (XMCD) technology [44, 31]. This for the first time experimentally shows that α"-$Fe_{16}N_2$ phase has a dual

electron configuration. We believed that neither itinerant nor localized magnetism alone can satisfyingly describe the magnetism in α”-$Fe_{16}N_2$ phase, and there seems to appear a considerable charge density difference inside and outside the Fe-N octahedral clusters shown in the Figure 2.3 due to the N atom reduced symmetry in the α”-$Fe_{16}N_2$ phase in the octahedral cluster. Using the Local Spin Density Approximation with on-site Coulomb (U) correction (LDA+U) calculation that illustrates the necessary features of the proposed physical configuration, a giant saturation magnetization simulation result, which is very close to the experimental results, was obtained.

2.5 Review of α”-$Fe_{16}N_2$ - Material Growth Methods

Iron nitride films that are thinner than 1000 $\mathring{A}$ and contain different percentages single crystal α”-$Fe_{16}N_2$ phase and nano-particle materials are the main research materials in the giant saturation magnetization α”-$Fe_{16}N_2$ phase research field. In the review of Metzger et. al. [45], they addressed to believe that epitaxial films of α”-$Fe_{16}N_2$ material can be prepared as pure phase, even with some doubts. But the powder of α”-$Fe_{16}N_2$ material could not yet be prepared as pure phase. Research shows the saturation magnetization magnitude of the samples contained α”-$Fe_{16}N_2$ phase does not depend on the thickness of the sample, which means the giant saturation magnetization should come from the bulk material magnetic property of α”-$Fe_{16}N_2$ phase, and has no relation with the thin film magnetic property [15]. This implies the thick sample that contains more α”-$Fe_{16}N_2$ phase will not enhance the saturation magnetization of it [46, 47], but only takes more time and

cost. These are the main reasons that most current α”-$Fe_{16}N_2$ research works are focusing on thin film samples instead of powder or bulk ones.

The most common α”-$Fe_{16}N_2$ thin film crystal growth technologies include thermal or molecule beam evaporation [8, 12, 13, 15, 16, 17], DC magnetron sputtering with nitrogen or ammonia gas atmosphere annealing [48, 31, 32]. And for nano-particle growth, nitriding of Fe_3O_4, Fe_2O_3, $Fe_{92}B_8$ or $Fe_{91}B_8Cu_1$ nano-particle in NH_3 or NH_3+H_2 gas atmosphere is the main technology [49, 50, 28, 29, 51].

For each crystal growth method, the experimental conditions, such as crystal growth temperature control, substrate material, material impurity, nitrogen gas partial pressure and vacuum pressure, even radio-frequency field in RF sputtering and deposit speed, may influence the crystal structure, magnetic property, even existence of α”-$Fe_{16}N_2$ phase in the iron nitride crystal. This makes uniform single crystal α”-$Fe_{16}N_2$ material extremely hard to grow, and also may be the main reason that none of the material growth process from current reported results is easily repeated and the material properties from different research works are inconsistent.

For the α”-$Fe_{16}N_2$ deposition substrate selections, several different material are chosen. Kim and Takahashi deposited pure Fe thin film on the glass substrate, and then grew α”-$Fe_{16}N_2$ on top of Fe layer [8]. This is one of the most common choices for later research [9, 11, 52]. GaAs or InGaAs is another common choice as substrate material. First, Fe or

Ag layer is deposited on GaAs or InGaAs substrate, then the Fe-N film containing α"-$Fe_{16}N_2$ phase grows on top of that [12, 13, 14, 15, 38, 16, 35, 53, 25, 26, 27, 31, 32]. Some other research select MgO as the substrate material because they worry about high mobility of In and As atoms may cause the diffusion problem in the interface between substrate and Fe-N layers [10, 54, 55, 56, 57, 58, 23, 59, 36]. As a common substrate material, Si is also selected by some research [21, 37, 60, 61]. And there are also some other substrate choices, such as, NaCl and Al_2O_3 [24, 22], but they are not commonly used. Here, it needs to mention that the substrate material crystalline orientation may be different in different research even the same material is selected.

Inoue et. al. first researched the enhancement of α"-$Fe_{16}N_2$ phase by Co additions [57]. It was found that the Fe-10 at.% Co alloy enhanced the formation amount α"-$Fe_{16}N_2$ three times than pure iron, and at the same time increased the formation temperature for 50 °C. Takahashi et. al. further researched not only the Co but also H additions on the α"-$Fe_{16}N_2$ phase formation [47]. It was found that the stable phase formation of α"-$(Fe_{100-X}Co_X)_{16}N_2$ (X=10-30) is very difficult through the ordering process of N atoms by post annealing. And it is not like the Co additions can obviously increase the magnetization of pure Fe, the Co additions only very slightly increase the magnetization of α"-$Fe_{16}N_2$. It was also found that the added H_2 can only accelerate the nitride speed of Fe atoms, and would not influent the magnetization value. Recently, Atiq et. al. researched the effect of Co, Pt and Cr additions on α"-$Fe_{16}N_2$ formation and magnetization [61]. It was found that the saturation magnetization always decreased with contents of Co, Pt and Cr additions

increased, which is different with Takahashi's conclusion for Co additions.

From the early Kim and Takahashi research, the effect of vacuum pressure and nitrogen gas partial pressure during the deposition on the saturation magnetization of material was noticed. It was found the material with largest saturation magnetization value was deposited in a specific vacuum pressure range, which was ~ 0.5 mTorr in nitrogen atmosphere. Gao et. al. noticed that the nitrogen flow rate during sputtering also influenced the saturation magnetization of iron nitride compound that included α"-$Fe_{16}N_2$ phase [52]. Tian et. al. [25], Li et. al. [60] also discussed or noticed the effect of nitrogen gas pressure or content during different deposition processes on the different iron nitrides deposition. Recently, Atiq et. al. found the different nitrogen partial pressures during deposition generated different iron nitride components, such as Fe_3N, γ′-Fe_4N and α"-$Fe_{16}N_2$. And only at about nitrogen partial pressure equaled to 0.8 mTorr, almost pure α"-$Fe_{16}N_2$ phase material was obtained and the largest saturation magnetization value was achieved. And most of other research only used some specific nitrogen partial pressures or contents or flow rate to deposit the α"-$Fe_{16}N_2$ material [31, 32].

Different material growth technologies, different substrates, different working gases, different material deposition ratios and temperatures and different annealing conditions from previous reported works are summarized in Table 2.1. And phase components and overall saturation magnetizations of thin film or powder samples, based on different material growth technologies are given in Table 2.2. The α"-$Fe_{16}N_2$ phase percentages in

iron nitrides are given by different characterization methods, therefore the Ms of α”-$Fe_{16}N_2$ phase can be calculated. By now, there is not a commonly agreed optimum and consistent deposition condition on α”-$Fe_{16}N_2$ phase material. This is the main reason of the achieved material properties are not reliable in different reported results.

Author	Method	Gas	Substrate	Thickness Å (Rate and Temp)
Kim et al, 1972	Evaporation	N_2	Glass	500 (10 Å/s @ RT)
Nakajima et al, 1989 a, b, 1990	Ion Implantation	N_2	MgO	2000 (N/A)
Komuro et al, 1990	Molecular Beam Epitaxy	N_2+NH_3	GaAs	70-1000 (0.04, 0.1, 1-10 Å/s @ 150 °C)
Sugita et al, 1991, 1993, 1994, 1996	Molecular Beam Epitaxy	N_2+NH_3	$In_{0.2}Ga_{0.8}As$	300-1000 (0.004-0.05 Å/s @ 150 °C)
M. Takahashi et al, 1993, 1994, 1996	Facing Target DC Magnetron Sputtering	Ar+N_2	MgO	300-10000 (1-5 Å/s @ RT)
Gao et al, 1993	Radio-frequency Sputtering	Ar+N_2	Glass	2000-2500 (2.6 Å/s @ RT)
Wallace et al, 1994	Fe 950 K Nitriding + Quenching	NH_3+H_2		Powder
Inoue et al, 1994	Sputtering	NH_3+H_2	MgO	5000 (N/A, nitride @ 500 °C)
Jiang et al, 1994	Ion-beam Sputtering	N_2	GaAs	3500 (2-3 Å/s @ RT)
Ortiz et al, 1994	DC Sputtering	Ar+N_2	MgO	200-850 (0.2 Å/s @ RT)
Okamota et al, 1996 a, b, 2000	Sputter Beam	Ar+N_2	GaAs	200-4000 (4-4.2 Å/s @ RT)
Sun et al, 1996, 1997	Facing Target Sputtering	Ar+N_2	NaCl	280-720 (2.0 Å/s @ 150 °C)
Brewer et al, 1996, 1997	DC Magnetron Sputtering	Ar+N_2	Si	600-1000 (0.5 Å/s @ 45 °C)
Weber et al, 1997	Ion Beam Implantation	N_2	Si	1550 (N/A)
Yao et al, 1998	Ion-beam Sputtering	N_2	GaAs	2000-5000 (2-3 Å/s @ RT)
H. Takahashi et al, 1999	Molecular Beam Epitaxy	N_2+NH_3	$In_{0.2}Ga_{0.8}As$	340-830 (0.01 Å/s @ 200-240 °C)
Wang et al, 2000	DC Magnetron Sputtering	Ar+N_2	Glass	2000 (1.1 Å/s @ RT)
Borsa et al, 2003	Molecular Beam Epitaxy	N atom flux	MgO	420 (Post nitride @ 200 °C)
Abdellateef et al, 2003	Thermalized Plasma DC Sputtering	Ar+N_2	Al_2O_3	1000-7000 (0.5 Å/s @ RT and 300 °C)
Tang et al, 2004, 2008, 2009	Fe-B 810-900 K Nitriding + Quenching	NH_3+H_2		Nanocrystal in amorphous ribbon
Sasaki et al, 2005	NanoCAP	NH_3		Nanoparticle
Li et al, 2006	RF Assistant Magnetron Sputtering	Ar+N_2	Si	N/A (N/A @ RT)
Kita et al, 2007	Fe_3O_4 723 K Nitriding + Quenching	NH_3+H_2		Nanoparticle
Kikkawa et al, 2008	Fe_2O_3 400 K Nitriding	NH_3		Powder
Atiq et al, 2009	DC Magnetron Sputtering	Ar+N_2	Si	400 (0.88 Å/s @ 200 °C)
Oku et al, 2009	Fe_3O_4 Nitriding	NH_3		Nanoparticle
Liu et al, 2009	Facing Target DC Magnetron Sputtering	Ar+N_2	Si + SiO_2	500 (N/A)

Table 2.1. Different material growth technologies, different substrates, different working gases, different material deposition ratios and temperatures and different annealing conditions are applied, in order to achieve α"-$Fe_{16}N_2$ phase.

Author	Phase	4πMs of Total (@ RT)	Bs of α" (@ RT)	α" Volume % (Cal. Method)
Kim et al, 1972	α + α"	2.5 T	2.8 T	50-80 (Ms vs T)
Nakajima et al, 1989 a, b, 1990	α + α' + α"	2.3 T	2.4 T	30 (XRD + Mössbauer)
Komuro et al, 1990	α + α"	2.66 T	2.8-3.0 T	85 (XRD + TEM)
Sugita et al, 1991, 1993, 1994	α"	2.9 T	2.9 T	100 (XRD)
M. Takahashi et al, 1993, 1994	α + α' + α"	2.0-2.15 T	2.25 T	23-36 (XRD + Mössbauer)
Gao et al, 1993	α + α" + γ'	2.1 T	2.95 T	18 (XRD + TEM)
Wallace et al, 1994	α + α" + γ	1.77 T	2.67 T	
Inoue et al, 1994	α + α"	N/A	N/A	N/A (XRD)
Jiang et al, 1994	α + α"	2.2 T		55 (XRD)
Ortiz et al, 1994	α' + α"	2.34 T		46 (XRD)
Okamota et al, 1996 a, b, 2000	α' + α"	2.5-2.6 T		32 (XRD + Mössbauer)
Sun et al, 1996	α"	2.78 T	2.78 T	100 (XRD)
Brewer et al, 1996, 1997	α' + α"	2.25 T		46 (XRD)
Weber et al, 1996	α + α' + α"		2.42 -2.45 T	70 (XRD + Mössbauer)
Yao et al, 1998	α + α"	2.2 T		N/A (XRD)
H. Takahashi et al, 1999	α"	2.98 T	2.98 T	100 (XRD)
Wang et al, 2000	α + α" + γ'	2.3 T		N/A (XRD)
Borsa et al, 2003	α + α" + γ'			22.1 (Mössbauer)
Abdellateef et al, 2003	α"+ γ+ ζ+ ε+ FeO	0.0097-1 T		N/A (XRD)
Tang et al, 2004, 2008, 2009	α + α" or α" + γ'	2.35-2.44 T		54 (XRD)
Sasaki et al, 2005	α + α"+ Fe_3O_4	0.8 T		N/A (XRD +XPS + TEM)
Li et al, 2006	α"+ ε			N/A (GIXRD)
Kita et al, 2007	α"+ amorph.Fe_xO	1 T	1.8 T	N/A (XRD + Mössbauer +TEM)
Kikkawa et al, 2008	α"	2.1 T	2.1 T	100 (XRD + Mössbauer)
Atiq et al, 2009	α"	2.3 T	2.3 T	100 (XRD)
Oku et al, 2009	α + α"+ Fe_3O_4	0.85 T	1.97 T	N/A (SANS)
Liu et al, 2009	α' + α"	2.39 T	2.96 T	30 (XRD)

Table 2.2. Phase components and overall saturation magnetizations of thin film or powder samples are different based on different material growth technologies. And α"-$Fe_{16}N_2$ phase percentages in iron nitrides are also given based on different characterization methods, therefore the Ms of α"-$Fe_{16}N_2$ phase are calculated.

2.6 Chemically Order-Disorder Phase Transformation and Johnson-Mehl-Avrami Equation

Johnson–Mehl–Avrami (JMA) theory is often used to estimate the order-disorder phase transformation by using an activation energy value [62]. For an isothermal phase transformation process, the relationship between the ordering parameter and the annealing time can be expressed as:

$$x(t) = 1 - \exp(-kt^n), \tag{2}$$

where x is the ordering parameter ($0 \leq x \leq 1$), t is the annealing time, n is the Avrami exponent and k is related with the new phase nucleation and growth during the phase transformation process. k can be further expressed as:

$$k = k_0 \exp(-E_a K^{-1} T^{-1}), \tag{3}$$

where k_0 is a temperature-independent parameter, E_a is the activation energy of the phase transformation, K is the Boltzmann constant and T is the annealing temperature.

Consider the strain energy during the phase transformation process, which can be written as,

$$E_s = E\varepsilon^2 V(1-\upsilon)^{-1}, \tag{4}$$

where E_s is the strain energy, E and υ are the Young's modulus and Poisson's ratio of the material, ε is the strain and V is the mole volume of the material. If there is a certain amount of initial strain during order-disorder phase transformation, which may be caused

by different phase lattice mismatching or lattice mismatching between thin film and substrate material, the existence of strain, therefore strain energy, will obviously influence the activation energy in Eqn. 3, and so that influence the phase transformation process. This has been found in a variety of alloy systems, when the alloys are transferred form one phase to the other under external pressures [63].

Now let us consider the phase transformation between α'-Fe_8N (disordered) to α"-$Fe_{16}N_2$ (ordered). We will use an in-situ annealing method to achieve α"-$Fe_{16}N_2$ phase from the as-deposited Fe_8N phase. For the as-deposited Fe_8N/underlayer/substrate sample, because of the lattice mismatch between Fe-N layer and the underlayer, there always exists a certain level of strain energy that is generated by the initial strain. This strain will change the activation energy and therefore influence the ordering parameter of this sample after its post-annealing for a possible α'-Fe_8N to α"-$Fe_{16}N_2$ phase transformation. It is reasonable to assume the dependence of the activation energy on the initial strain energy of this material as:

$$E_a = E_0 + E_s \,, \tag{5}$$

where E_0 is the activation energy value when there is no initial strain caused by any lattice mismatch or other reasons. Combine eqns. 4 and 5, the activation energy can be further written as,

$$E_a = E_0 + A(a - a_0)^2, \tag{6}$$

where a is the in-plane lattice parameter of the as-deposited sample, a_0 is the in-plane lattice parameter without any material deformation, and

$$A = EVa_0^{-2}(1-\upsilon)^{-1} \quad (7)$$

is a constant related with material physical properties.

By using Fe-N thin films that contain partial α"-$Fe_{16}N_2$ phase ordering parameter data, which can be calculated from XRD patterns by eqn. (1), under different in-situ annealing temperature and time, the unknown parameters in the expression of JMA can be obtained. Therefore, the optimum annealing temperature and time for the phase transformation from α'-Fe_8N to α"-$Fe_{16}N_2$ can be estimated. Furthermore, the α"-$Fe_{16}N_2$ phase aging process, which is the reverse transformation from α"-$Fe_{16}N_2$ to α'-Fe_8N can also be estimated.

Chapter 3

Experimental Apparatus

All Fe-N samples in our experiments were prepared by DC magnetron facing-target sputtering (FTS) technique, which was first developed by Naoe et. al. [64]. Figure 3.1 shows the technical configuration of FTS.

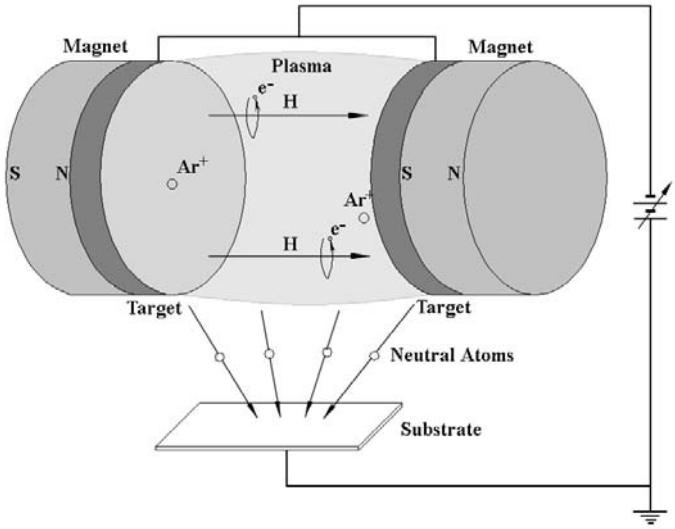

Figure 3.1. The technical configuration of FTS is shown with details. The high density plasma and high energy electrons are constrained between two targets by applied magnetic field.

In the structure, two pieces of targets with same size and material are arranged parallel and facing each other. The high negative sputtering voltage is applied at the surfaces of both targets. The applied magnetic field with proper intensity is perpendicular to the surface of targets. Under the co-action of applied sputtering voltage and magnetic field,

the plasma will be confined between the two targets. Comparing with ordinary DC magnetron target sputtering technology, the FTS have several advantages. First, FTS can achieve higher deposition rate under same sputtering conditions for both nonmagnetic material and magnetic material. Because the confined electrons can improve the ionization of the working gas between targets and increase the amount of sputtering ions. This will increase the sputtering speed. Especially for ferromagnetic material deposition, for the ordinary DC magnetron sputtering technique, the applied magnetic field upon the target surface is shorted by the ferromagnetic target. This reduces the ionization upon the surface of target and drops the deposition rate dramatically. But for FTS method, the magnetic field between two targets is always homogeneous with a high intensity, which makes the ferromagnetic thin film deposition ratio much higher than ordinary DC sputtering. Second, during FTS deposition process, the particles that deposition on the substrate are all neutral atoms, because both ions and electrons are confined between the facing targets by the magnetic field, and the substrate is out of sputtering plasma. This will obviously minimize the deposition defect. Without the high-energy ions and electrons bombard on the substrate, the temperature increasing of the substrate during sputtering process is minimized. Of course, the sputtering target cost in FTS will be doubled, and the device setup is more complicated than ordinary DC magnetron sputtering.

Since the FTS technique can be used to deposit both ferromagnetic and nonferromagnetic thin films with higher deposition ratio and better defect and temperature control, it is

widely used today in thin film preparation [65, 66, 67, 68, 69, 70, 71, 72, 73, 74, 75, 76, 77, 78, 79, 80, 81, 82].

There are two sets of DC magnetron FTS systems locating in Department of Electrical and Computer Engineering laboratory 6-138 of University of Minnesota. One is a single-pair (Fe) facing-target sputtering system (SFTSS), the other is a multiple-pair facing-target sputtering system (MFTSS) that includes three pairs of facing-targets. And all majority experiments are finished in the SFTSS, because the MFTSS is still partially under construction. In this chapter, both systems will be introduced with details.

3.1 Single Facing-Target Sputtering System

Figure 3.2 shows the outside view of the SFTSS. And the technical configuration is shown in Figure 3.3.

In Figure 3.3, the top configuration is the top view of chamber inside details, and the bottom configuration is the cross-section view along the middle axis of the system. The SFTSS is made up of three sub-systems. The first sub-system includes one 15-inch diameter chamber and one small load-lock. The load-lock can only be used to load one piece of sample each time. Between the main chamber and load-lock, there is a high-vacuum manual gate valve that used to keep the vacuum condition of main chamber during load-lock opening for sample loading and unloading. There is a vertical oriented

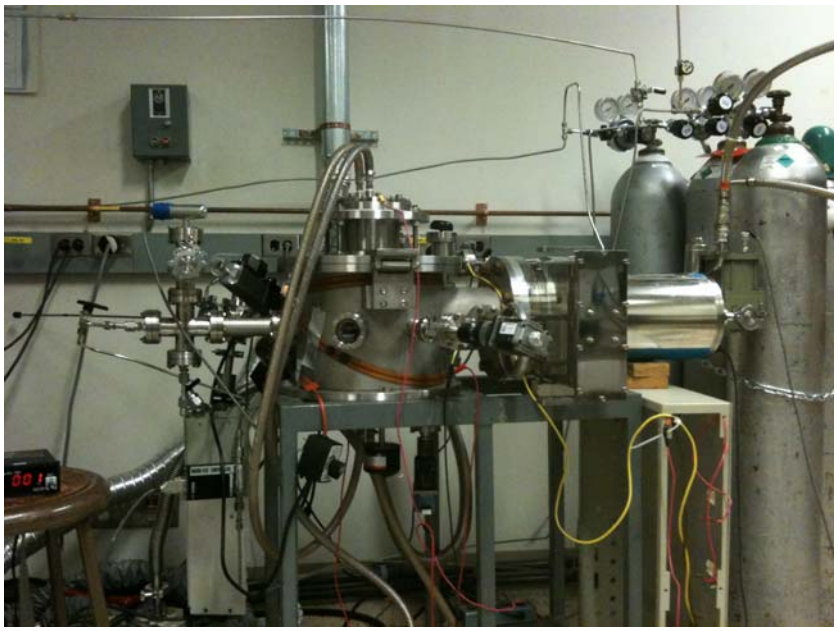

Figure 3.2. The Single Facing-Target Sputtering System is located in laboratory 6-138 in Department of Electrical and Computer Engineering, and the outside view of the system is shown here.

sample stage. The sample will be transferred from load-lock by a sample transfer beam and plate, which is attached on load-lock, and set up on the sample holder on the stage. And the sample's preheating and in-situ annealing are both finished by the sample heater, which is a heating light bulb at the back of the sample holder. The heating light bulb input voltage can be adjusted by a set of Sorensen DCR60-9B DC power supply. And the relationship between the sample heater input voltage and the final stable heating temperature has been calibrated. So the preheating and post-annealing temperature can be controlled accurately. The second sub-system is the pair of Fe facing targets, which is used to deposit Fe underlayer and Fe-N thin film. The pair of facing targets includes two

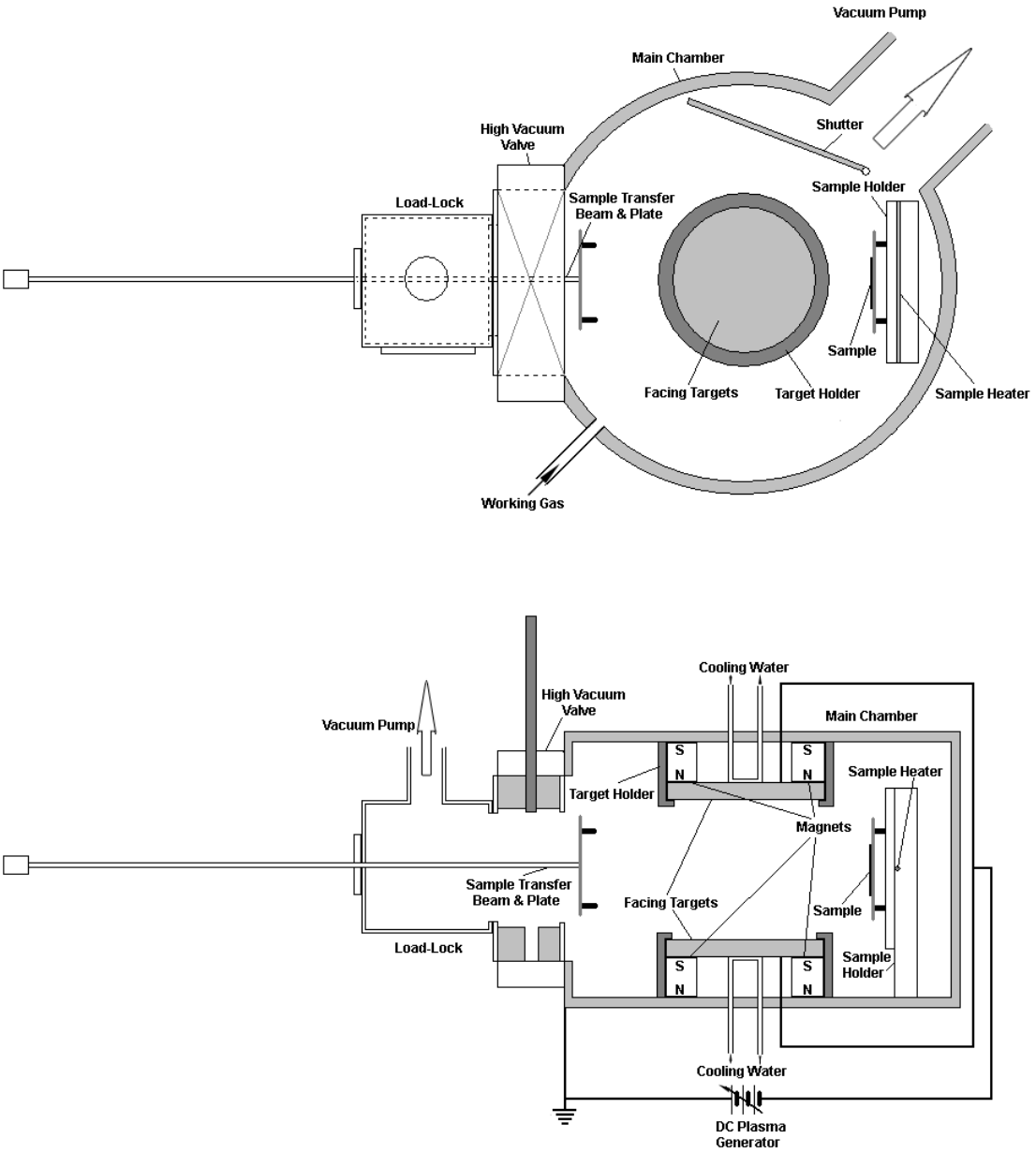

Figure 3.3. The SFTSS technical configurations of top view and side cross-section view are shown.

pieces of 99.99% purity Fe targets, and they are both 4 inches in diameter and 0.125 inch in thickness. The distant between these two targets is about 4 inches. At the backside of either target, there is one piece of ring-shape strong magnet. And the distribution of south poles and north poles are shown in the figure. The pair of magnets will provide magnetic field that normal to the surfaces of targets, then to constrain the high-speed ions during sputtering, therefore to control the amount and ultimate energy of Fe atoms that deposit on the substrate. The high negative sputtering voltage of targets is provided by a set of ENI DCG-100 DC plasma generator. Either the sputtering plasma power, the sputtering voltage or the sputtering current can be preset through the plasma generator to satisfy the experimental requirements. And during sputtering process, the facing targets are cooled down by the water-cooling circuits at the back of them to avoid overheat. The facing targets and main chamber are electrically insulated by two pieces of Teflon, which keep the main chamber (includes sample stage) and other parts of SFTS system electrical grounded condition during sputtering. And the positive power side of plasma generator is also grounded. The third sub-system is the vacuum system, which includes three stages vacuum pumps. The first stage is a Leybold AEG mechanical pump, which can pump the pressure of load-lock and main chamber below $5*10^{-2}$ Torr and satisfy the starting requirement of the second stage, Leybold TurboVac50 turbomolecular pump. The turbomolecular pump can ultimately vacuum the pressure of chamber and load-lock below 10^{-6} Torr, and reach the pressure level to operate the third stage vacuum pump, a set of CTI Cryogenics Cryo-Torr8 pump. After the three-stage vacuum process, the base pressure of Fe-N thin film deposition can be kept lower than $1.5*10^{-7}$ Torr (~$2.0*10^{-5}$

Pa). Besides these three sub-systems, there are also some other additional devices in the SFTS system, such as working gas flow controllers, vacuum monitors including low-vacuum rough gauges and high vacuum ion gauges, shutter for sample pre-sputtering protection, etc.

3.2 Multiple Facing-Target Sputtering System

Figure 3.4 shows the outside view of MFTSS in lab 6-138, which is still partially under construction now.

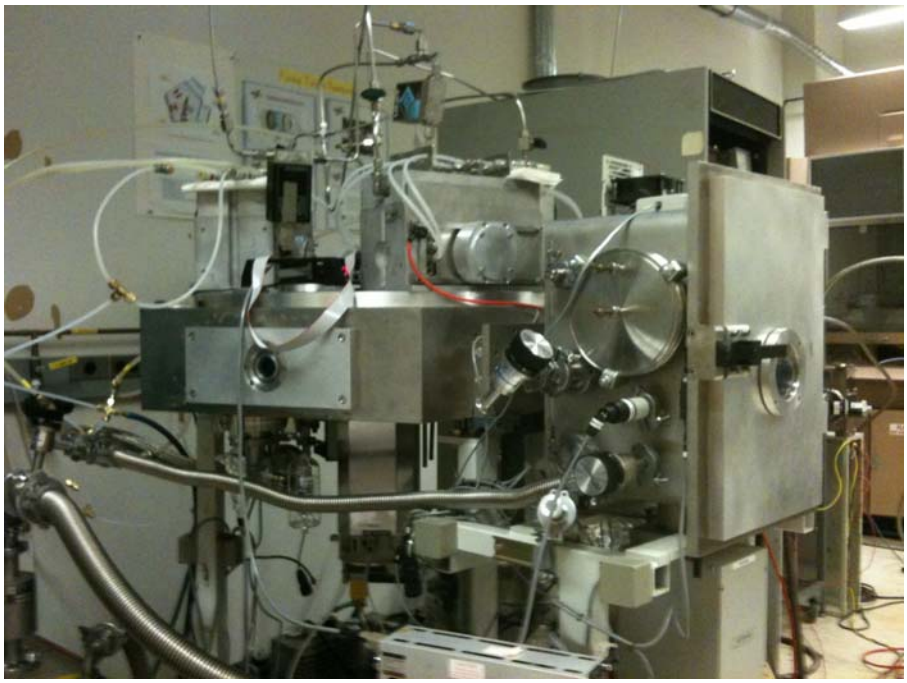

Figure 3.4. The Multiple Facing-Target Sputtering System is also located in laboratory 6-138, and the outside view of the system is shown above.

In Figure 3.5, the technical detail is shown in the configuration. First, the top configuration shows the top outside view of the MFTSS, and the bottom one shows the cross section view along view plane A-B of the system. Similar with SFTSS, the MFTSS is also mainly made up of three sub-systems.

The first sub-system includes a pentagon chamber, and a large load-lock. There are several differences between MFTSS and SFTSS for this sub-system. First, in MFTSS, the load-lock can load multiple pieces of samples each time, but in SFTSS, the load-lock can only load one piece each time. Second, the sample transfer beam is attached with the load-lock in SFTSS, but is attached and in the main chamber in MFTSS. And the sample is set up at a fixed position in the chamber of SFTSS, but can be relocated in different positions in the chamber of MFTSS depending on the sputtering targets choice. Third, the sample preheat and in-situ annealing in SFTSS are both finished in the chamber without sample transfer needed, but because the sample heaters are located in the load-lock in MFTSS as shown in Figure 3.5, sample needs to be preheated in the load-lock and transferred into chamber for thin film deposition, and then transferred back to load-lock for post-annealing. For the second sub-system, sputtering facing-targets, there are three pairs of exchangeable facing targets. All targets are 3 inches in diameter and 0.0625 inch in thickness. Currently, one pair of 99.995% purity Fe targets, one pair of 99.995% purity Ag targets and one pair of 99.99% purity Cr targets are set in the system. Each target is fixed in a copper target stage. Two target stages with same targets are placed face-to-face in a rectangular shape target holder, and the working gas is also designed to flow into the

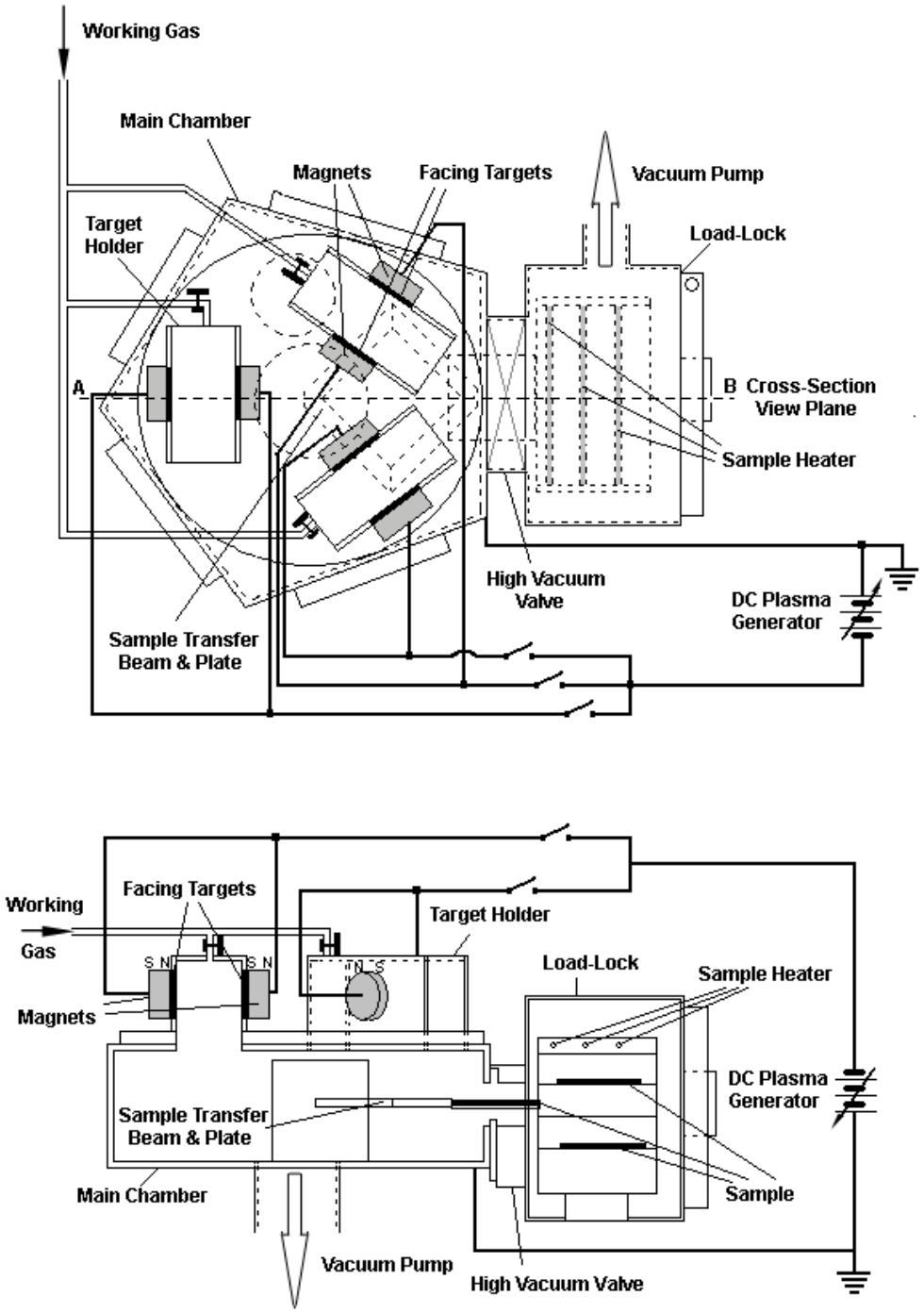

Figure 3.5. The technical details about the MFTSS are shown in the configuration above, and the configuration includes top view and side cross-section view.

target holder to generate plasma during sputtering. The sputtering voltage is applied to targets through the stages and the targets are also cooled by the water-cooling circuits inside the stages during sputtering to prevent targets overheat. Each set of target and stage are electrical insulted by a Teflon plate with the holder, therefore insulated with the whole body of the chamber. Same as SFTSS, at the backside of each target stage in MFTSS, there is one strong cylinder 3 inches diameter magnet that used to apply magnetic field between the surfaces of each pair of facing targets. The setting of north poles and south poles of magnets can be seen in Figure 3.5. The sputtering plasma is also generated by a set of ENI DCG-100 plasma generator. In MFTSS, the vacuum sub-system also includes three stages vacuum pumps. The first one is an Edwards E2-80 mechanical pump, which is used to vacuum system below $5*10^{-2}$ Torr pressure level. After the second stage Pfeiffer TMU065 turbomolecular drag pump vacuuming, the pressure level can reach 10^{-6} Torr level. After running the CTI cryogenics APD cryopump for a while, the base pressure can reach 10^{-7} Torr level to satisfy the high quality thin film deposition base pressure requirement.

There is one important issue in MFTSS, which doesn't exist in SFTSS. That is the facing targets may be contaminated during other targets sputtering. A shutter plate is used to prevent this problem, which is set up to attached the chamber cover and can be rotated parallel to the chamber cover plane. There is a rectangular open area in the shutter plate, which has the same size with the bottom open of target holders. When one pair of the facing targets is selected to sputter, the open area will be rotated manually to match the

target holder and let plasma sputter into chamber. At the same time, because the shutter plate covers the other two pairs of facing targets, they will be kept clean.

Comparing the SFTSS and MFTSS, it can be seen that the utilization of SFTSS has some limitations. First, because only Fe targets are located in SFTSS, which is required by Fe-N thin film sputtering, this limits the choice of underlayer material. From previous reported work by Okamoto et. al. [35, 53, 27], it is found that the existence and selection of underlayer are very important the achievement of high magnetic moment Fe-N thin films that contain partially α"-$Fe_{16}N_2$ phase. And also from their results, it can be seen that Ag underlayer helps the formation of α"-$Fe_{16}N_2$ phase better than Fe underlayer under same Fe-N thin film deposition conditions. But in our SFTSS, without further modification, there is no way to in-situ deposit other material underlayer except Fe. The same limitation exists in the selection of capping layer that used to prevent Fe-N oxidizing. Second, the sample position in the chamber is fixed in SFTSS, which makes the search for optimum deposition distant under different deposition conditions very hard. When the sample is too far from sputtering plasma, the deposition ratio will drop dramatically, and may be too slow. But if the sample is too near to the plasma, the plasma may contact with sample, which will increase the substrate temperature and deposition defects as ordinary DC magnetron sputtering. So the optimum of sample position related with the plasma is very important for FTS method. Third, when one sample's deposition is finished and is in-situ annealed, the other sample can't be deposition at the same time. This will limit the efficiency of large amount samples preparation. All these limitation

can be well overcome by MFTSS. For the first one, because there are three pairs of facing targets in the MFTSS, one pair targets can be selected as Fe for Fe-N layer deposition. Then, the second pair of targets can be selected as Ag for underlayer deposition, and the third pair of Cr targets is used to cap the Fe-N thin film to prevent oxidizing. If other materials are selected to optimize underlayer or capping layer, these two pairs of targets can be replaced easily. For the second one, the sample transfer beam can adjust sample distance to the plasma in the chamber manually as experiment design, which makes optimum deposition position be easily obtained. For the third one, after one sample deposition is finished, it can be transferred into load-lock for post annealing, then, another sample can be transferred into chamber at once for a new round of thin film deposition. And the process is same for more samples as long as the number of samples doesn't exceed the limitation of load-lock.

Multiple facing-target sputtering system can be further modified for radio-frequency (RF) facing-target sputtering in the future for non-conductible material depositions, such as metallic oxidization depositions. It needs to notice that the electrical insulation layers for non-conductible targets should be much thicker than those for conductible targets, the minimum thickness of insulation layers needs to be obtained from calculation based on RF sputtering power.

Chapter 4

$Fe_{16}N_2$ Sample Preparation and Characterization

4.1 Fe-N Sample Preparation by Magnetron DC Facing Target Sputtering System

In our samples, a series of Fe-N/Fe films were sputtered on GaAs (001) single crystal substrates by using the SFTSS. The single crystal (001) GaAs substrates (2 inches wafers) were bought from AXT inc., the technical details of the low defect GaAs wafer can be found through their website [83]. First, the Fe (002) underlayer was deposited on GaAs (001) substrate to induce the Fe-N texture. For different samples, the thicknesses of Fe underlayer are different and vary from 18 to 24 nm. The substrate temperature was fixed at 250 ˚C during Fe underlayer deposition. Argon gas with 99.995% purity was used as sputtering gas. Deposition rate of Fe films was about 2.0 $\overset{0}{A}$/s when the working pressure is about 5 mTorr. The Fe-N layer was subsequently deposited by sputtering the Fe facing targets with an appropriate Ar_2 and N_2 mixture gas at room temperature. The ratio of Ar_2 and N_2 for α'-Fe_8N deposition is about 100:2.4. Deposition rate was calibrated as about 1.6 $\overset{0}{A}$/s with 0.12 mTorr N_2 partial pressure, Ar_2 partial pressure is still fixed as 5 mTorr. Base pressure was kept at $\leq 1.5\times10^{-7}$ Torr. After the film's deposition, Fe-N/Fe/GaAs samples were in-situ annealed at 150 ˚C for 1-40 hrs. When the annealing was finished, samples were taken out of chamber, labeled, and ready for characterization and measurement.

The crystal structures were characterized by using a Siemens D5005 X-ray diffractometer (XRD) with Cu Kα radiation source. M-H loops and saturation magnetization values were obtained at room temperature for fields up to 10 kOe that was applied in-plane using a Princeton Vibrating Sample Magnetometer (VSM). Films' thickness was measured by a Philips X'Pert Pro X-ray Diffractometer and selectively confirmed by cross-sectional transmission electron microscopy.

4.2 Characterizations of Fe-N Samples

Figure 4.1 shows the X-ray diffraction spectra of as-deposited Fe_8N sample and in-situ post-annealed Fe_8N with partial $Fe_{16}N_2$ phase sample. In the figure, the fingerprint (002) group peak for $Fe_{16}N_2$ phase can be clearly seen, which proves the existence of α"-$Fe_{16}N_2$ phase after the in-situ annealing process.

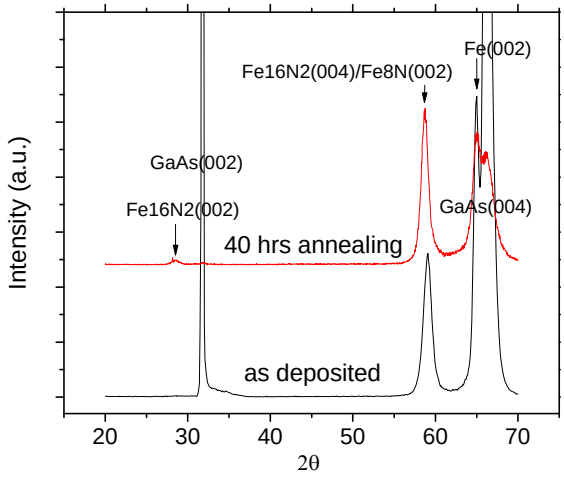

Figure 4.1. X-ray diffraction spectra of as-deposited Fe_8N sample and in-situ post-annealed Fe_8N with partial $Fe_{16}N_2$ phase sample are shown in the same figure for comparison.

Figure 4.2 gives the magnetic hysteresis loops of the as-deposited Fe_8N/Fe/GaAs sample and post-annealed (Fe_8N+$Fe_{16}N_2$)/Fe/GaAs sample. Also the M-H loop for the GaAs substrate with only Fe underlayer sample is shown in the figure for a comparison.

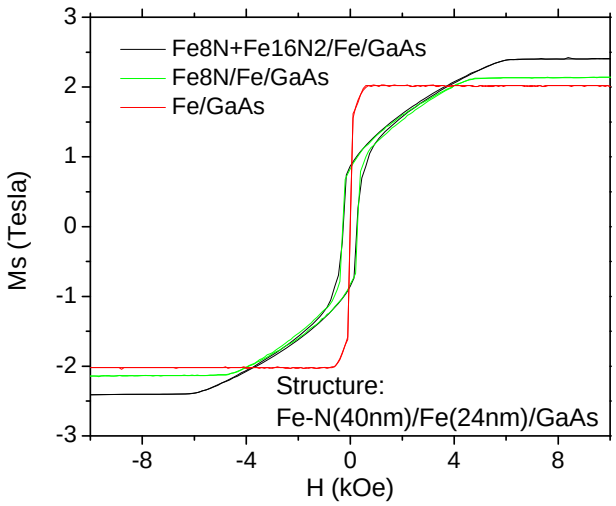

Figure 4.2. Magnetic hysteresis loops of the as-deposited Fe_8N/Fe/GaAs sample and post-annealed (Fe_8N+$Fe_{16}N_2$)/Fe/GaAs sample are shown in the figure, also a loop of the sample with only Fe/GaAs is shown for comparison.

The M_s value of the Fe-N/Fe/GaAs sample in Figure 4.2 was calculated based on the total moment of both Fe-N layer (~50 nm) and Fe underlayer (~24 nm) divided by the total volume of both layers. The Ms value of Fe/GaAs film was found around 2.04 T. By subtracting the net moment contribution from Fe/GaAs, the saturation magnetization value of α'-Fe_8N phase in the as-deposited Fe_8N/GaAs samples was found around 2.0-2.2 T. The Ms value of the Fe-N layer of the in-situ annealed Fe-N/Fe/GaAs samples, which has the mixed phases of Fe_8N+$Fe_{16}N_2$, was found up to ~2.6 T. Considering a relatively

low volume ratio of $Fe_{16}N_2$ phase in Fe-N layer (~30%, which can be calculated from XRD intensity integrate from Eqn. 1), a much higher saturation magnetization value of α"-$Fe_{16}N_2$ phase should be extracted. This is consistent with what in Sugita's reports.

Figure 4.3 shows the dependence of the ordering parameter of the samples with Fe_8N+$Fe_{16}N_2$ mixed phases on the post-annealing time at 150 ˚C annealing temperature. Here, the ordering parameter was obtained by calculating the XRD intensity integrated ratio in Eqn. 1. It can be seen that the ordering parameter of Fe-N mixed phase increases nonlinearly and most like exponentially with the annealing time.

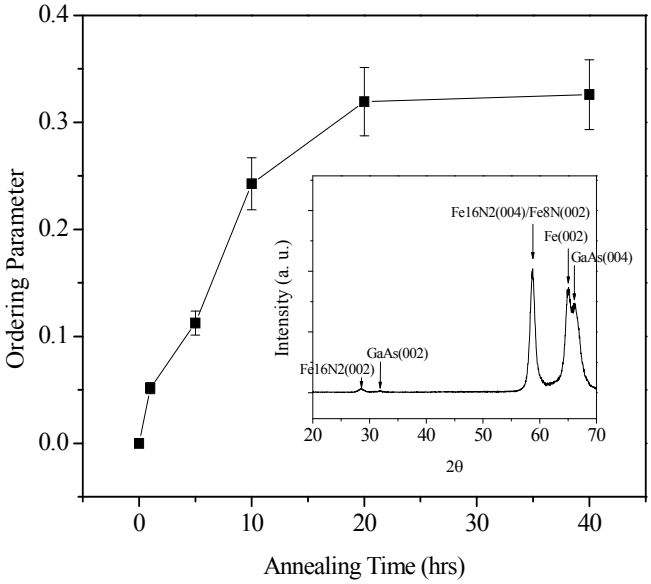

Figure 4.3. Dependence of the ordering parameter of the Fe_8N samples with partial $Fe_{16}N_2$ phases on the post-annealing time at the same 150 ˚C annealing temperature is shown here.

Figure 4.4 shows the XRD spectra of Fe-N/Fe/GaAs samples with different Fe-N and Fe thicknesses. The peaks of Fe_8N and Fe phases were labeled. It can be seen that the in-

plane lattice parameters are different for Fe-N layer with different Fe-N and Fe layer thicknesses. This lattice difference was caused by the lattice mismatch between the BCC Fe layer (002) plane (a=2.87 $\overset{0}{A}$) and the GaAs (001) plane (a=2.825 $\overset{0}{A}$), also between the Fe underlayer and the Fe-N layer (a= ~2.86 $\overset{0}{A}$, c= ~3.145 $\overset{0}{A}$). And this initial strain exists after deposition and will influence the disordering-ordering phase transformation of Fe-N layer during annealing process.

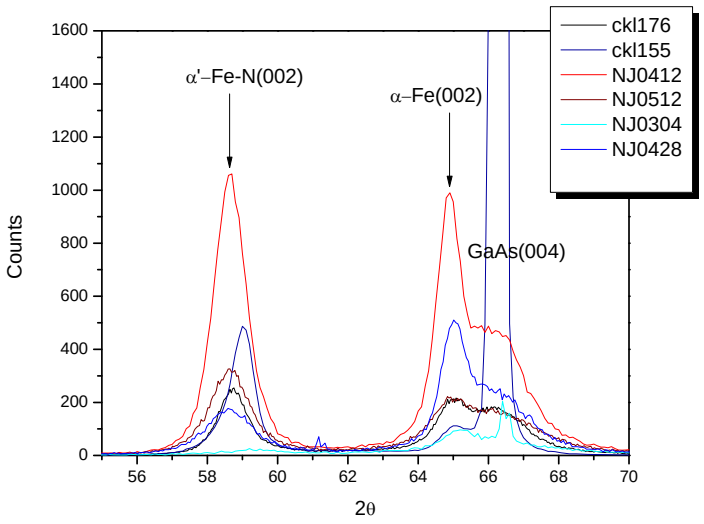

Figure 4.4. XRD spectra of Fe-N/Fe/GaAs samples with different Fe-N and Fe thicknesses show the in-plane lattice parameters of Fe-N layers are different.

Table 4.1 summarizes the details of the lattice parameters, post-annealing time and ordering parameters of the Fe-N layer for the samples with different layer thicknesses.

Sample ID	Fe Layer Thickness (nm)	Fe-N Layer Thickness (nm)	a (Å)	c (Å)	Anneal Time (hrs)	Ordering Parameter
ckl176	18	40	2.86847	3.14316	40	0.36
ckl155	24	150	2.86847	3.12764	30	0.05
NJ0304	24	20	2.85791	3.11229	20	0.08
NJ0412	24	40	2.86926	3.14364	10	0.11
NJ0428	24	40	2.86690	3.14804	20	0.14
NJ0512	24	50	2.87005	3.13975	30	0.23

Table 4.1. A series of Fe-N/Fe/GaAs samples were prepared with different Fe-N and Fe layer thicknesses and they were also post-annealed with different times. After annealing, each sample was characterized by XRD to obtain the ordering parameter and in-plane lattice parameter.

Chapter 5

Order-Disorder Phase Transformation Analysis

Based on the sample characterization results in Table 4.1, the α'-Fe_8N to α"-$Fe_{16}N_2$ order-disorder phase transformation process can be analyzed through the Johnson–Mehl–Avrami (JMA) equation.

Consider the Eqns. 2 and 3 (in chapter 2.6), there are three unknowns in JMA equation. The first one is the Avrami exponent n, the second is the temperature-independent parameter k_0, and the third one is the activation energy E_a, which is also temperature independent. From the relationship between ordering parameter and annealing time, Avrami exponent n can be fitted out as

$$n = 0.5967 \tag{8}$$

at 150 ˚C and the coefficient of determination is

$$R^2 = 0.94242. \tag{9}$$

From the value of coefficient of determination, it can be seen that the ordering parameter after different annealing times follows JMA equation well.

It can be also noted from JMA equation that it is impossible to fit the temperature-independent parameter k_0 out under only one annealing temperature condition. So a relationship of ordering parameter and annealing time under different annealing temperature from the work of Okamota et. al. [35] is used to fit k_0 here. In their paper,

they claimed that a largest ordering parameter of 0.32 in Fe-N mixed phase was achieved after 100 hours annealing at 200 ˚C. Since 200 ˚C is near the annealing temperature we used in our experiments (150 ˚C), the Avrami exponent n will not change much. So here the Avrami exponent n is still assumed as 0.5967 at 200 ˚C. Then the constant of k_0 can be calculated out as

$$k_0 = 1.3355 \times 10^{-3}. \tag{10}$$

Take this value into the expressions of E_a in eqn. (6), by using the in-plane lattice parameter data in Table 4.1, three unknown constant in the expression of activation energy can be fit out as:

$$a_0 = 2.86308 \pm 0.00140 \overset{0}{\text{A}}, \tag{11}$$

$$A = 2183.3 \pm 528.1\, eV/(\overset{0}{\text{A}})^2, \tag{12}$$

and

$$E_0 = 0.0515 \pm 0.0129\, eV. \tag{13}$$

Here, it can be seen that the activation energy of α'-Fe_8N to α"-$Fe_{16}N_2$ phase transformation is about two times larger than the atomic thermal fluctuation energy (~0.025 *eV*) when there is no initial strain before the phase transformation. This is an important parameter for the following discussion.

Now let us consider about the energy level of each Fe-N phase. It is easy to know that the disordered Fe_8N phase is at lower energy level and ordered $Fe_{16}N_2$ phase is at higher one. The energy barrier between these two phases is defined as the activation energy of the phase transformation, which could be affected by the initial strain energy *Es* built in the

sample as discussed above. At room temperature, for α'-Fe_8N phase, this energy barrier is too high to overpass simply by a thermal fluctuation process ($\sim 0.025\ eV$ vs $\sim 0.052\ eV$ as calculated above). Thus α'-Fe_8N phase is stable at room temperature. At a higher temperature, such as annealing at 150-200 ˚C, α'-Fe_8N phase can gain enough energy to overpass the above calculated energy barrier and transform into α"-$Fe_{16}N_2$ phase, but it will never transform into a pure $Fe_{16}N_2$ phase (x=1 in Eqn. 2) even with a very long annealing time. From JMA theory, it is noticed that a higher temperature will help the transformation of α'-Fe_8N phase into α"-$Fe_{16}N_2$ phase. However, unfortunately, with higher annealing temperatures, Fe-N layer will be transformed to other phases, such as γ'-Fe_4N [6]. So the choice of the annealing temperature is very critical for the Fe_8N-$Fe_{16}N_2$ phase transformation. Meanwhile, there is a probability for a reverse phase transformation process, since the energy barrier is lower for the phase transformation from the Fe_8N to $Fe_{16}N_2$ phase and the $Fe_{16}N_2$ phase has a higher equilibrium energy level of itself. This will enable the α"-$Fe_{16}N_2$ phase transformation back to α'-Fe_8N phase, even at room temperature. Figure 5.1 shows the Fe_8N+$Fe_{16}N_2$ sample decay time vs. α"-$Fe_{16}N_2$ phase activation energy at room temperature with different ordering parameters from 0.1 to 0.9. This decay effect is also named as the aging effect. Now our model can be used to address some arguments and shed the light on the inconsistency in previous α"-$Fe_{16}N_2$ reports. For example, some researchers found that α'-Fe_8N layer could be well deposited but only very small amount of α"-$Fe_{16}N_2$ phase could be obtained through post-annealing [52]. Based on our model, this may be caused by a bad choice of substrate, which could provide a large initial strain energy, therefore a large activation

energy to prevent the phase transformation from α'-Fe_8N to α"-$Fe_{16}N_2$ phase. One key experimental report on the non-existence of the giant Ms in α"-$Fe_{16}N_2$ phase was given in reference [56], in which the researchers obtained α"-$Fe_{16}N_2$ phase with a high ordering parameter (characterized by XRD) by different sputtering processes including the FTS process but only found its saturation magnetization around α'-Fe_8N level (measured by VSM). This has been quoted as one of main results to be inconsistent with MBE grown α"-$Fe_{16}N_2$. Based on our model, assume the reverse activation energy from α"-$Fe_{16}N_2$ to α'-Fe_8N is 60% of that from α'-Fe_8N to α"-$Fe_{16}N_2$, using the lattice parameter in their report, the activation energy from α"-$Fe_{16}N_2$ phase to α'-Fe_8N phase is only about 0.03 *eV*, and this will make their α"-$Fe_{16}N_2$ sample with high ordering parameter (0.36) transform back to α'-Fe_8N in less than 34.5 hours as shown in Figure 5.1. This may imply their samples had partially or fully transformed back to Fe_8N phase before they were measured by VSM. At the same time, the ordering parameter of Sugita's MBE grown α"-$Fe_{16}N_2$ samples is very close to 1. As shown in Figure 5.1, it can be seen that if their sample's activation energy is above 0.05 *eV* (this is very possible if there exists a large strain energy after α"-$Fe_{16}N_2$ phase is cooled down to room temperature after post annealing for MBE method), the decay time of their samples will be as long as months. This explains the Sugita's MBE grown α"-$Fe_{16}N_2$ sample could show more stable magnetization during the characterization period. But even for their sample, it would transform back to α'-Fe_8N phase in a long time later.

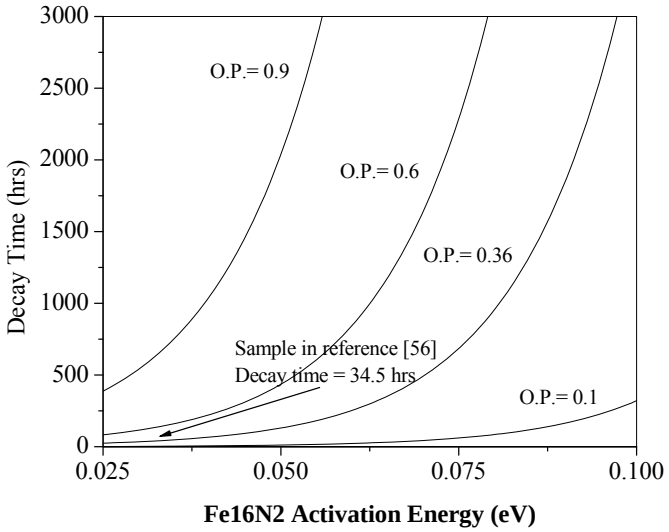

Figure 5.1 The relationship between Fe_8N+$Fe_{16}N_2$ mixed phase sample decay time and material activation energy at room temperature condition with different ordering parameter is shown.

Chapter 6

Conclusions and Some Thought for Future Research

During my one-year EE Master Degree study, I have finished two things: 1) set up a three-pair of facing-target sputtering system (MFTSS); 2) studied the phase transformation mechanism between Fe_8N and $Fe_{16}N_2$;

Through my quantitative analysis, I discovered the following: 1) Initial strain between the Fe-N layer and the template that is used to grow Fe-N layer changed the activation energy level of the phase transformation and thus influenced the Fe_8N-$Fe_{16}N_2$ transformation process. The choice of the substrate and the underlayer material is very critical for the epitaxial growth of Fe-N layer; 2) Choice of the post-annealing temperature was found also very important. A proper annealing temperature should not only help the transformation from the α'-Fe_8N phase to α"-$Fe_{16}N_2$ phase by overpassing the energy barrier, but also prevent the formation of other Fe-N phases; 3) It is impossible to achieve pure α"-$Fe_{16}N_2$ phase through annealing an α'-Fe_8N phase. The final ordering parameter of α"-$Fe_{16}N_2$ was decided by its initial lattice strain, annealing temperature and annealing time; 4) Inconsistency of the reported α"-$Fe_{16}N_2$ results on the giant saturation magnetization was explained based on our proposed model, which was part of aging effect or reverse phase transformation process from α"-$Fe_{16}N_2$ phase with giant saturation magnetization to α'-Fe_8N phase with normal saturation magnetization.

In the future research, first, the FTS deposited α'-Fe_8N samples will be annealed under different annealing temperatures and annealing times, then the ordering parameter of each sample will be measured carefully. Therefore, the Avrami exponent *n* under different temperature can be obtained accurately. Then the error bar for the activation energy may be minimized. Also, this group of experiments will help optimize the annealing temperature. Second, the lattice mismatch data for the samples with different underlayer and Fe-N layer thicknesses needs to be carefully measured. And it is also very important for the best underlayer material and thickness hunting. Third, to avoid the aging effect of α"-$Fe_{16}N_2$ phase is the most practical challenge for achieving giant saturation magnetization Fe-N samples with long-term reliability. We need to search methods to stabilize α"-$Fe_{16}N_2$ phase without quick aging to satisfy the industrial application requirements.

Reference

1. R. O'Handley, (2000), *Modern Magnetic Materials Principles and Applications*. John Wiley and Sons, Inc., USA.

2. A. Sakuma, (1991), Self-consistent calculations for the electronic-structure of iron nitride, Fe3N, Fe4N and Fe16N2. *J. Magn. Magn. Mater.*, 102: 127.

3. C. Chang, J. Sivertsen and J. Judy, (1987), Structure and magnetic-properties of RF reactively sputtered iron nitride thin-films. *IEEE Trans. Magn.*, 23: 3636.

4. A. Leineweber, H. Jacobs, F. Huning, H. Lueken, H. Schilder and W. Kockelmann, (1999), ε-Fe3N: magnetic structure, magnetization and temperature dependent disorder of nitrogen. *J. Alloys Comp.*, 288: 79.

5. J. -P. Wang, (2010), (invited) Perpendicular Magnetic Recording Conference (PMRC), May, Sendai, Japan; (invited) Information Storage Industry Consortium (INSIC), January, Berkeley; American Physical Society March Meeting, March, Portland.

6. K. Jack, (1951), The occurrence and crystal structure of α"-iron nitride; a new type of interstitial alloy formed during the tempering of nitrogen-martensite. *Proc. R. Soc. London*, A208: 200.

7. M. Usikov and A. Khachaturyan, (1970), Structure and morphology of an ordered α" phase in the Fe-N system. *Fiz. Metal. Metal.*, 30: 614.

8. T. Kim and M. Takahashi, (1972), New magnetic material having ultrahigh magnetic moment. *Appl. Phys. Lett.*, 20: 492.

9. K. Nakajima, S. Okamoto and T. Okada, (1989), Formation of ferromagnetic iron nitrides in iron thin films by high-dose nitrogen ion implantation. *J. Appl. Phys.*, 65: 4357.

10. K. Nakajima and S. Okamoto, (1989), Nitrogen-implantation-induced transformation of iron to crystalline Fe16N2 in epitaxial iron films. *Appl. Phys. Lett.*, 54: 2536.

11. M. Russak, C. Jahnes, E. Klohln, J. Lee, M. Re and B. Webb, (1991), Magnetic and structural characterization of sputtered FeN multilayer films. *J. Appl. Phys.*, 70: 6427.

12. M. Komuro, Y. Kozono, M. Hanazono and Y. Sugita, (1990), Epitaxial growth and magnetic properties of FeN films with high saturation magnetic flux density (invited). *J. Appl. Phys*., 67: 5126.

13. Y. Sugita, K. Mitsuoka, M. Komuro, H. Hoshiya, Y. Kozono and M. Hanazono, (1991), Giant magnetic moment and other magnetic properties of epitaxially grown Fe16N2 single-crystal films (invited). *J. Appl. Phys*., 70: 5977.

14. H. Takahashi, K. Mitsuoka, M. Komuro and Y. Sugita, (1993), Anomalous Hall resistivities of single-crystal Fe16N2 and Fe-N martensite films epitaxially grown by molecular beam epitaxy. *J. Appl. Phys*., 73: 6060.

15. Y. Sugita, H. Takahashi, M. Komuro, K. Mitsuoka and A. Sakuma, (1994), Magnetic

and M8ssbauer studies of single-crystal Fe16N2 and Fe-N martensite films epitaxially grown by molecular beam epitaxy (invited). *J. Appl. Phys*., 76: 6637.

16. Y. Sugita, H. Takahashi, M. Komuro, M. Igarashi, R. Imura and T. Kambe, (1996), Magnetic and electrical properties of single-phase, single-crystal Fe16N2 films epitaxially grown by molecular beam epitaxy (invited). *J. Appl. Phys*., 79: 5576.

17. H. Takahashi, M. Igarashi, A. Kaneko, H. Miyajima and Y. Sugita, (1999), Perpendicular uniaxial magnetic anisotropy of Fe16N2 [001] single crystal films grown by molecular beam epitaxy. *IEEE Trans. Magn*., 35: 2982.

18. J. Coey, K. O'Donnell, Q. Qi, E. Touchais and K. Jack, (1994), The magnetization of α"Fe16N2. *J. Phys. Condens. Matter*., 6: L23.

19. J. Coey, (1994), The magnetization of bulk α"Fe16N2 (invited). *J. Appl. Phys*., 76: 6632.

20. W. Wallace and M. Huang, (1994), Enhanced Fe moment in nitrogen martensite and Fe16N2 (invited). *J. Appl. Phys*., 76: 6648.

21. T. Weber, L. de Wit, F.W. Saris and P. Schaaf, (1996), Search for giant magnetic moments in ion-beam-synthesized α"-Fe16N2. *Thin Solid Films*, 279: 216.

22. M. Abdellateef, C. Heiden, H. Lemke, F. El-Hossary and K. Baerner, (2003), Magnetic properties and structure of the α"-Fe16N2 films. *J. Magn. Magn. Mater*., 256: 214.

23. C. Ortiz, G. Dumpich and A. Morrish, (1994), Epitaxial Fe16N2 films grown by sputtering. *Appl. Phys. Lett*., 65: 2737.

24. D. Sun, E. Jian, M. Tian, C. Lin and X. Zhang, (1996), Epitaxial single crystal Fe16N2 films grown by facing targets sputtering. *J. Appl. Phys*., 79: 5440.

25. M. Tian, E. Jiang and D. Sun, (1997), Fe-N gradient films and epitaxial Fe16N2 single-crystal films. *J. Vac. Sci. Tech*., A15(4): 2313.

26. Z. Yao, H. Jiang, Z. Liu, D. Huang, F. Qin, S. Zhu and Y. Sun, (1998), Formation and magnetic properties of Fe16N2 films prepared by ion-beam-assisted deposition. *J. Magn. Magn. Mater*., 177-181: 1291.

27. S. Okamoto, O. Kitakami and Y. Shimada, (2000), Crystal distortion and the magnetic moment of epitaxially grown α"-Fe16N2. *J. Magn. Magn. Mater*., 208: 102.

28. S. Kikkawa, A. Yamada, Y. Masubuchi and T. Takeda, (2008), Fine Fe16N2 powder prepared by low-temperature nitridation. *Mater. Res. Bulle*., 43: 3352.

29. W. Liu, J. Tang and Y. Du, (2008), Nanocrystalline soft magnetic ribbon with α"-Fe16N2 nanocrystallites embedded in amorphous matrix. *J. Magn. Magn. Mater*., 320: 2752.

30. M. Takahashi and H. Shoji, (2000), α"-Fe16N2: giant magnetic moment or not? *J. Magn. Magn. Mater*., 208: 145.

31. N. Ji, X. Q. Liu and J.-P. Wang, (2010), Theory of giant saturation magnetization in α"-Fe16N2: role of partial localization in ferromagnetism of 3d transition metals. *New J. Phys.,* 12: 063032.

32. N. Ji, Y. Wu and J.-P. Wang, (2010), J. Appl. Phys., Under review.

33. H. Wriedt, N. Gokcen and R. Nafziger, (1992), *ASM Online Handbook*.

34. H. Tanaka, S. Nagakura, Y. Nakamura and Y. Hirotsu, (1997), Electron crystallograghy study of tempered iron-nitrogen martensite and structure refinement of precipated α"−$Fe_{16}N_2$. *Acta Mater*., 45: 1401.

35. S. Okamoto, O. Kitakami and Y. Shimada, (1996), Characterization of epitaxially growth Fe-N films by sputter beam method. *J. Appl. Phys*., 79: 1678.

36. D. Borsa and D. Boerma, (2003), Phase identification of iron nitrides and iron oxynitrides with Mössbauer spectroscopy. *Hyper. Inter*., 151: 31.

37. M. Brewer, C. Echer, K. Krishnan, T. Kobayashi and A. Nakanishi, (1997), Magnetic and physical microstructure of Fe16N2 films grown epitaxially on Si (001). *J. Appl. Phys*., 81: 4128.

38. H. Jiang, K. Tao and H. Li, (1994), The thermostability of the Fe16N2 phase deposited on a GaAs substrate by ion-beam assisted deposition. *J. Phys. Condens. Matter*., 6: L279.

39. J. Kanamori, (1990), Interplay between electronic structure and correlation through

the sd mixing in transition metal system. *Prog. Theo. Phys. Supp*., 101: 1.

40. R. Coehoorn, G. Daalderop and H. Jansen, (1993), Full-potential calculations of the magnetization of Fe16N2 and Fe4N. *Phys. Rev*., B48: 3830.

41. S. Asano and M. Yamaguchi, (1997), Band calculations of interstitially modified iron and rare-earth iron compounds. *Physica*, B237: 541.

42. W. Lai, Q. Zheng and W. Hu, (1994), The giant magnetic moment and electronic correlation effect in ferromagnetic nitride Fe16N2. *J. Phys. Condens. Matter*., 6: L259.

43. A. Sakuma, (1996), Electronic and magnetic structure of iron nitride, Fe16N2 (invited). *J. Appl. Phys*., 79: 5570.

44. X. Liu, Y. Xu, C. Sanchez-Hanke and J.-P. Wang, (2009), Discovery of localized states of Fe 3d electrons in Fe16N2 and Fe8N films: an evidence of the existence of giant saturation magnetization. *arXiv:0909.4478*.

45. R. Metzger, X. Bao and M. Carbucicchio, (1994), Magnetism of α"−$Fe_{16}N_2$ (invited), *J. App. Phys*., 76: 6626.

46. M. Brewer, K. Krishnan and C. Ortiz, (1996), Epitaxial Fe16N2 films grown on Si (001) by reactive sputtering. *J. App. Phys*., 79: 5321.

47. M. Takahashi, H. Takahashi, H. Nashi. H. Shoji, T. Wakiyama and M. Kuwabara (1996), Structure and magnetic moment of α"-$Fe_{16}N_2$ compound films: Effect of Co and H on phase transformation (invited). *J. Appl. Phys*. 79: 5564.

48. X. Wang, W. Zheng, H. Tian, S. Yu, W. Xu, S. Meng, X. He, J. Han, C. Sun and B. Tay, (2003), Growth, structural and magnetic properties of iron nitride thin films deposited by DC magnetron sputtering. *App. Surf. Sci*., 220: 30.

49. J. Tang, A. Wu, K. Peng and Y. Du, (2004), Formation of nanocrystalline Fe-N-B-Cu soft magnetic ribbons. *J. Non-Cryst. Solids*, 337: 276.

50. E. Kita, K. Shibata, H. Yanagihara, Y. Sasaki and M. Kishimoto, (2007), Magnetic properties of core-shell type Fe16N2 nanoparticles. *J. Magn. Magn. Mater.*, 310: 2411.

51. T. Oku, T. KiKuchi, T. Shinohara, J. Suzuki, Y. Ishii, M. Takeda, K. Kakurai, Y. Sasaki, M. Kishimoto, M. Yokoyama and Y. Nishihara, (2009), Small-angle polarized neutron scattering study of spherical Fe16N2 nano-particles for magnetic recording tape. *Physica*, B404: 2575.

52. C. Gao, W. Doyle and M. Shamsuzzoha, (1993), Quantitative correlation of phase structure with the magnetic moment in RF sputtered Fe-N films. *J. Appl. Phys*., 73: 6579.

53. S. Okamoto, O. Kitakami and Y. Shimada, (1996), α"-$Fe_{16}N_2$ phase epitaxially grown by sputter beam method. *J. Appl. Phys*., 79: 5250.

54. K. Nakajima and S. Okamoto, (1990), Large magnetization induced in single crystalline iron films by high-dose nitrogen implantation. *Appl. Phys. Lett*., 56: 92.

55. M. Takahashi, H. Shoji, H. Takahashi, T. Wakiyama, M. Kinoshita and W. Ohta, (1993), Synthesis of Fe16N2 films by using reactive plasma. *IEEE Trans. Magn*., 29:

3040.

56. M. Takahashi, H. Shoji, H. Takahashi, H. Nashi, T. Wakiyama, M. Doi and M. Matsui, (1994), Magnetic moment of α"-$Fe_{16}N_2$ (invited). *J. Appl. Phys*., 76: 6642.

57. Y. Inoue, S. Takebayashi and T. Mukai, (1994), Enhancement of the formation of Fe16N2 on Fe films by Co additions. *J. Appl. Phys*., 76: 6653.

58. Y. Takahashi, H. Shoji and M. Takahashi, (2000), Impurity effect of carbon on structure and saturation magnetization of Fe-N films. *J. Magn. Magn. Mater*., 210: 333.

59. S. Grachev, D. Borsa, S. Vongtragool and D. Boerma, (2001), The growth of epitaxial iron nitrides by gas flow assisted MBE. Surf. Sci., 482-485: 802.

60. W. Li, F. Zheng and W. Fei, (2005), Effect of assistant RF field on phase composition of iron nitride film prepared by magnetron sputtering process. *J. Vac. Sci. Tech.*, A(24)1: 170.

61. S. Atiq, H. Ko, S. Siddiqi and S. Shin, (2009), Preparation and the influence of Co, Pt and Cr additions on the saturation magnetization of α"-$Fe_{16}N_2$ thin films. *J. Alloys Comp*., 479: 755.

62. D. Porter and K. Easterling, (1992), *Phase Transformations in Metals and Alloys*, 2nd ed. Taylor & Francis, Boca Raton/London.

63. R. Hazen and A. Navrotsky, (1996), Effect of pressure on order-disorder reactions. *Am. Mineral*., 81: 1021.

64. M. Naoe, S. Yamanaka and Y. Hoshi, (1980), Facing targets type of sputtering method for deposition of magnetic metal films at low temperature and high rate. *IEEE. Trans. Magn.,* 16(5): 646.

65. M. Naoe, Y. Hoshi, S. Yamanaka and M. Kume, (1983), Preparation of high-coercivity Co-Pt alloy films by target-facing type of high rate sputtering. *Jpn. J. Appl. Phys.,* 22: 1519.

66. K. Sumiyama, Y. Hirose and Y. Nakamura, (1990), Structural and magnetic-properties of nonequilibrium disordered Fe-Al alloys produced by facing-target type DC sputtering. *Jpn. J. Phys. Soc.,* 59(8): 2963.

67. J. Roth, (1990), Sputtering of limiter and divertor materials. *J. Nucl. Mater.,* 176: 132.

68. E. Lacroix, P. Gerard, G. Marest and M. Dupuy, (1991), Substrate effect on the crystalline orientation of barium hexaferrite films. *J. Appl. Phys.*, 59(8): 2963.

69. K. Sin, J. Sivertsen, and J. Judy, (1994), Surface roughness and magnetic-properties of in-situ heated and postannealed thin-films of perpendicular barium ferrite. *J. Appl. Phys.*, 75(10): 5972.

70. K. Tominaga, M. Kataoka, T. Ueda, M. Chong, Y. Shihiro and I. Mori, (1994), Preparation of conductive ZnO: Al films by a facing target system. *Thin Solid Films*, 253(1-2): 9.

71. Y. Hoshi, Y. Kubota and M. Naoe, (1995), Control of orientation and crystallite size of barium ferrite thin-films in sputtering-deposition. *IEEE Trans. Magn.,* 31(6): 2782.

72. H. Bai, E. Jiang, C. Wang and D. Sun, (1996), Thermal evolution of carbon in annealed Co/C soft x-ray multilayers. *J. Appl. Phys.,* 80: 1428.

73 Z. Qian, G. Wang, J. Sivertsen and J. Judy, (1997), NiZn ferrite thin films prepared by facing target sputtering. *IEEE Trans. Magn.,* 33(5): 3748.

74. K. Tominaga, N. Umezu, I. Mori, T. Ushiro, T. Moriga and I. Nakabayashi, (1998), Properties of ZnO: In film prepared by sputtering of facing ZnO: In and ZnO targets. *J. Vac. Sci. Tech.,* A16(3): 1213.

75. X. Li, K. Yamashita, T. Tanaka, Y. Suzuki and M. Okuyama, (2000), Structural and electrical properties of highly oriented Pb(Zr,Ti)O3 thin films deposited by facing target sputtering. *Sens. and Actu.,* A82(1-3): 265.

76. H. Ma, J. Cho and C. Park, (2002), A study of indium tin oxide thin film deposited at low temperature using facing target sputtering system. *Surf. Coat. Tach.,* 153(2-3): 131.

77. K. Zhao and H. Wong, (2003), Epitaxial growth of platinum thin films on various substrates by facing-target sputtering technique. *J. Crys. Grow.,* 256: 283.

78. X. Wang, P. Wu, Z. Li, E. Jiang and H. Bai, (2005), Microstructure of amorphous carbon nitride thin films fabricated by facing-target reactive magnetron sputtering. *J. Phys.,* D37(15): 2127.

79. H. Kim, S. Kim, K. Lee and K. Kim, (2006), Direct Al cathode layer sputtering on LiF/Alq(3) using facing target sputtering with a mixture of Ar and Kr. *Appl. Phys. Lett.,* 88(8): 083513.

80. H. Fujiura and S. Nakagawa, (2007), Fabrication of CoCrPt-SiO2 films on exible tape substrate using facing target sputtering system. *J. Magn. Magn. Mater.,* 310(2): 2659.

81. J. Moon and H. Kim, (2008), Sputtering of aluminum cathodes on OLEDs using linear facing target sputtering with ladder-type magnet arrays. *J. Elect. Soc.,* 155(7): J187.

82 Y. Kim, S. Jin, S. Kim, Y. Choi, I Jeon and J. Han, (2008), Study on the electrical properties of ITO films deposited by facing target sputter depostion. *J. Phys.,* D42(7): 075412.

83. http://www.axt.com/